Highly efficient and stable p-type ZnO nanowires with piezotronic effect for photoelectrochemical water splitting

Chang Cao[a,b], Xinxin Xie[a,b], Yamei Zeng[a,b], Shaohua Shi[a,b], Guizhen Wang[a,b],

Liang Yang[b], Cai-Zhuang Wang[c], Shiwei Lin[a,b,*]

[a] State Key Laboratory of Marine Resource Utilization in South China Sea, Hainan University, Haikou 570228, P. R. China

[b] College of Materials Science and Engineering, Hainan University, Haikou 570228, P. R. China

[c] Ames Laboratory-U. S. Department of Energy, and Department of Physics and Astronomy, Iowa State University, Ames, IA 50011, USA

* Corresponding author. E-mail address: linsw@hainanu.edu.cn (S. Lin).

Abstract

Unremitting efforts have been made to develop high-performance photoelectrochemical (PEC) water-splitting system to produce clean hydrogen fuel using sunlight. In this work, a novel way, combining highly-ordered nanowires (NWs) structure and piezotronic effect of p-type ZnO has been demonstrated to dramatically enhance PEC hydrogen evolution performance. Systematic characterizations indicate that the Sb atoms uniformly dope into ZnO NWs and substitute Zn sites with the introduction of two zinc vacancies to form the shallow acceptor Sb_{Zn}-$2V_{Zn}$ complex. Detailed synchrotron-based X-ray absorption near-edge structure (XANES) experiments in O K-edge and Zn L-edge further confirm the formation of the complex, and theoretical calculation verifies the Sb^{5+} state dominating the complex. The optimal photocurrent density of the 0.2Sb/ZnO-anneal NWs can reach -0.85 mA/cm^2 (0 V_{RHE}) which is 17.2 times larger than that of the n-ZnO NWs under sunlight illumination (100 mW/cm^2). Furthermore, the piezotronic effect can be introduced to regulate the charge separation and transfer in the ZnO NWs through modulating the band structure near the interface. The photocurrent density can further increase to -1.08 mA/cm^2 (0 V_{RHE}) under

a 0.6% tensile strain, which is 27.4% enhancement with respect to the ZnO sample without strain. These results provide an efficient way to design and develop high-performance photoelectrodes toward PEC hydrogen evolution.

Keywords: P-type ZnO; Nanowires; Piezotronic effect; Photoelectrochemical; Hydrogen evolution

1. Introduction

Metal-oxide semiconductors have been widely investigated for applications in photocatalytic water splitting since the first demonstration in 1972 [1]. Among them, ZnO shows great potential for applications in hydrogen evolution systems, dye-sensitized solar cells, and photoelectric sensors on account of its excellent photoelectrochemical (PEC) activities, environmentally friendly nature and low-cost [2-5]. Successful preparation of p-n junction is often desirable to obtain highly efficient ZnO-based optoelectronic devices [6-7]. However, it is quite difficult to acquire p-type ZnO with great stability and low resistance under current conditions. The as-grown ZnO electrodes through a variety of methods usually exhibit n-type conductivity for the reason of intrinsic defects such as zinc interstitial (Zn_i) and oxygen vacancy (V_o) that stem from host lattice of ZnO and generate a large number of shallow donor levels [8,9]. The previous researches have also reported the poor stability of p-type ZnO, which is easy to convert into n-type conductivity at room temperature [10-13]. Not only the intrinsic donor defects, but also the deep acceptor levels and low acceptor doping solid solubility are the reasons why p-type doping ZnO is tough to achieve [13].

Recent experimental and theoretical reports showed that p-type ZnO could be produced with success through the group V elements doping [14-16]. Although nitrogen (N) was considered to be an ideal candidate for achieving p-type conductivity in ZnO from the viewpoint of electron configuration and solid solubility, few experimental results demonstrated stable and reproducible p-type N-doped ZnO nanostructure [17]. Moreover, antimony (Sb) and arsenic (As) have also been advised as anticipative doping candidates to realize p-type conductivity and large hole concentration. Instead of occupying the oxygen sites to form deep energy levels, Sb has been suggested to

form the Sb_{Zn}-$2V_{Zn}$ complex according to the recent experimental and theoretical analyses [18,19]. The major effort on the Sb-doped p-type ZnO was conducted on optimizing the material preparation process, improving photocatalytic dye degradation behavior, and understanding the relationship between the crystal/electrical structure and light emission properties [20,21]. Few studies have used p-type ZnO to improve PEC performance for the rational design of efficient photoelectrodes.

The separation of photo-induced charge carriers essentially shifts the positive and negative charges in opposite directions, thereby spatially isolating the oxidation reaction from the reduction reaction [22-23]. Based on this fact, a wide-range and high-intensity built-in electric field is the direct driving force that promotes efficient separation of electrons and holes for piezotronic semiconductors such as ZnO. The piezotronic effect can achieve such regulation of the charge separation and transfer process, which is an electromechanical coupling effect that enables the mutual conversion between mechanical energy and electrical energy [24-26]. This effect can stimulate the inner-crystal polarization of materials with mechanical energy to generate an internal electric field, which provides a new theory for modulating carriers transport through mechanical strain [27-29]. ZnO is a very outstanding and multifunctional material with both piezotronic effect and great semiconductor properties [30,31]. Wang et al. prepared a 100 nm long ZnO nanowire that could generate a potential difference of 0.4 V when subjected to a stress of 80 nN in the c-axis direction [32]. This potential difference was the core driving force that effectively facilitated carrier separation. On the basis of the piezotronic effect, a broad range of novel applications have recently been demonstrated in the devices like strain-gated transistors, optoelectronic devices, strain nanogenerators and solar cells [30,33-37]. However, it is still lack of applying piezotronic effect on p-type ZnO photoelectrode to reinforce the PEC behaviors. Such information is important not only for the comprehension of the universality of piezotronic effect in the p-type ZnO but also for the rational design and optimization of the photoelectrode for efficient PEC performance.

In this work, we successfully fabricated single-crystalline Sb-doped p-type ZnO NWs through a facile low-temperature hydrothermal method, and realized the

modulation of PEC performance by the piezotronic effect using our self-designed electrode clamp device. Here, we first report the combination of p-type conductivity and piezotronic effect in ZnO NWs to enhance PEC hydrogen evolution. Both experimental and theoretical analyses have been systematically conducted to show the direct evidence of the formation of the Sb_{Zn}-$2V_{Zn}$ complex in Sb-doped ZnO NWs as well as the role in the enhancement of photoelectrical properties. The charge carriers transfer process can be controlled by improving the crystal quality and altering the magnitude of applied strains on ZnO NWs to regulate PEC behaviors. Therefore, such results provide a facile and feasible approach to motivate the optoelectronic properties and applications based on the p-type piezotronic ZnO NWs.

2. Experimental section

2.1 Fabrication of undoped and Sb-doped ZnO NWs

The undoped and Sb-doped ZnO NWs were prepared on flexible stainless steel sheet substrate (0.15 mm) through a low-temperature hydrothermal method as shown in Fig. 1a [38,39]. The homogeneous and containable ZnO seed film was deposited onto the stainless-steel sheet by means of atomic layer deposition (ALD) [40] instead of the conventional sol-gel process. The thickness of ZnO seed layer could reach 30-35 nm after deposition. The substrates with the ZnO seed layer were then placed in the mixed solution at 95 ℃ for 24 h for hydrothermal synthesis. In a typical synthesis, the mixed solution for preparing the undoped ZnO NWs included 0.05 M zinc nitrate $(Zn(NO_3)_2 \cdot 6H_2O)$, 0.05 M hexamethylenetetramine (HMT) and 0.8 M ammonium hydroxide. For the sake of producing the Sb-doped ZnO NWs, a dopant solution was added to the above-mixed solution before heat treatment. The mixture containing equal molar sodium hydroxide (NaOH) and glycolic acid $(C_2H_4O_3)$ constituted the dopant solution, where antimony acetate $(Sb(CH_3COO)_3)$ was added in a molar ratio of 1:12. The Sb doping concentrations were changed between 0.1% and 1.0% mole percentage with respect to zinc. To further improve the crystal quality, the ZnO NWs samples were annealed at 500 ℃ for 1 h under argon atmosphere.

2.2 Characterization

The feature and microscopic structure of the ZnO NWs were characterized by

scanning electron microscope (FESEM, Hitachi SU8020) and transmission electron microscope (TEM, Tecnai G2 F20) with an energy-dispersion X-ray spectrometer (EDS). The crystalline phase of the photoelectrodes was examined using an X-ray diffractometer (XRD, Bruker D8) in the 2θ between 20° and 80° with Cu Kα radiation source. UV-vis spectrometer (Purkinje TU-1901) was used to investigate the optical performance of ZnO NWs, and the diffuse reflection contains specular reflection by using an integrating sphere and the reference material ($BaSO_4$). With the Kuelka-Munk transformation, the diffuse reflection spectrum can be converted to the absorption spectrum. Room-temperature Raman scattering was tested on Renishaw inVia Reflex spectroscopy used 514 nm laser source. Steady-state photoluminescence (PL) measurements of n-type and p-type ZnO NWs were conducted using Hitachi F-7000 FL spectrophotometer with the excitation wavelength at 325 nm. X-ray photoelectron spectrum (XPS) was analyzed using Thermo escalab 250Xi equipped with Al Kα radiation. Furthermore, synchrotron-based X-ray absorption near-edge structure (XANES) experiments in O K-edge and Zn L-edge of the samples were performed at the photoemission end station of beamline 10B in the National Synchrotron Radiation Laboratory (Hefei, China).

2.3 Photoelectrochemical measurements

The PEC properties of photoelectrodes were tested by an electrochemical workstation (Zahner Zennium) using a typical three-electrode system under 500 W Xe-lamp (AM 1.5 G, 100 mW/cm^2) illumination. A Pt foil and an Ag/AgCl electrode were applied to be the counter electrode and the reference electrode, respectively. The ZnO NWs was applied as the working electrode in the electrolyte solution containing 200 mM Na_2SO_4. The measured potential versus (vs) Ag/AgCl electrode was converted into that versus reversible hydrogen electrode (RHE) by the Nernst equation ($E_{RHE} = E_{Ag/AgCl} + 0.059 \text{ pH} + 0.196$). The linear sweep voltammetry (LSV) curve was tested with a scan rate of 10 mV/s. Electrochemical impedance spectroscopy (EIS) experiment was conducted by a 10 mV sinusoidal ac disturbance in a frequency range from 0.01 Hz to 100 kHz. H_2 evolution by the three-electrode system was tested at -0.2 V_{RHE} in 0.2 M Na_2SO_4 solution with methanol as sacrificial agent using a gas chromatography (TM

GC 7900, China).

2.4 Computational details

According to the density functional theory (DFT), the studies on the formation energy of defects for Sb doping ZnO NWs were accomplished with projected augmented wave pseudopotential (PAW) and generalized gradient approximation (GGA) using the Vienna Ab initio simulation package (VASP). A cutoff energy was 400 eV for plane wave expansion and $2 \times 3 \times 3$ K-point meshing was produced for optimizing the structure. For studying the defect complexes, a $5 \times 3 \times 2$ supercell was conducted as the majorization wurtzite structure ZnO.

3. Results and discussion

3.1 Undoped and Sb-doped ZnO NWs

ZnO NWs prepared with different Sb doping concentrations were applied as the photoelectrodes to exam PEC hydrogen evolution properties for the first time to the best of our knowledge, which can provide more possibilities to develop p-n junctions based devices [41]. Figs. 1 (b-d) show the typical SEM images of undoped ZnO NWs, 0.2 mol% Sb-doped ZnO NWs before and after thermal treatment (referred to as n-ZnO, 0.2Sb/ZnO and 0.2Sb/ZnO-anneal, respectively). The diameter of the undoped ZnO NWs is 90-100 nm on average and the nanowires are vertically scattered on the substrate (Fig. 1b). After Sb doping, the diameter of the ZnO NWs increases to about 120 nm with a certain degree of perpendicularity (Fig. 1c). After the thermal treatment, the surface of Sb-doped ZnO NWs looks smooth and the nanowires appear well-defined and densely-arranged, as clearly shown in Fig. 1d.
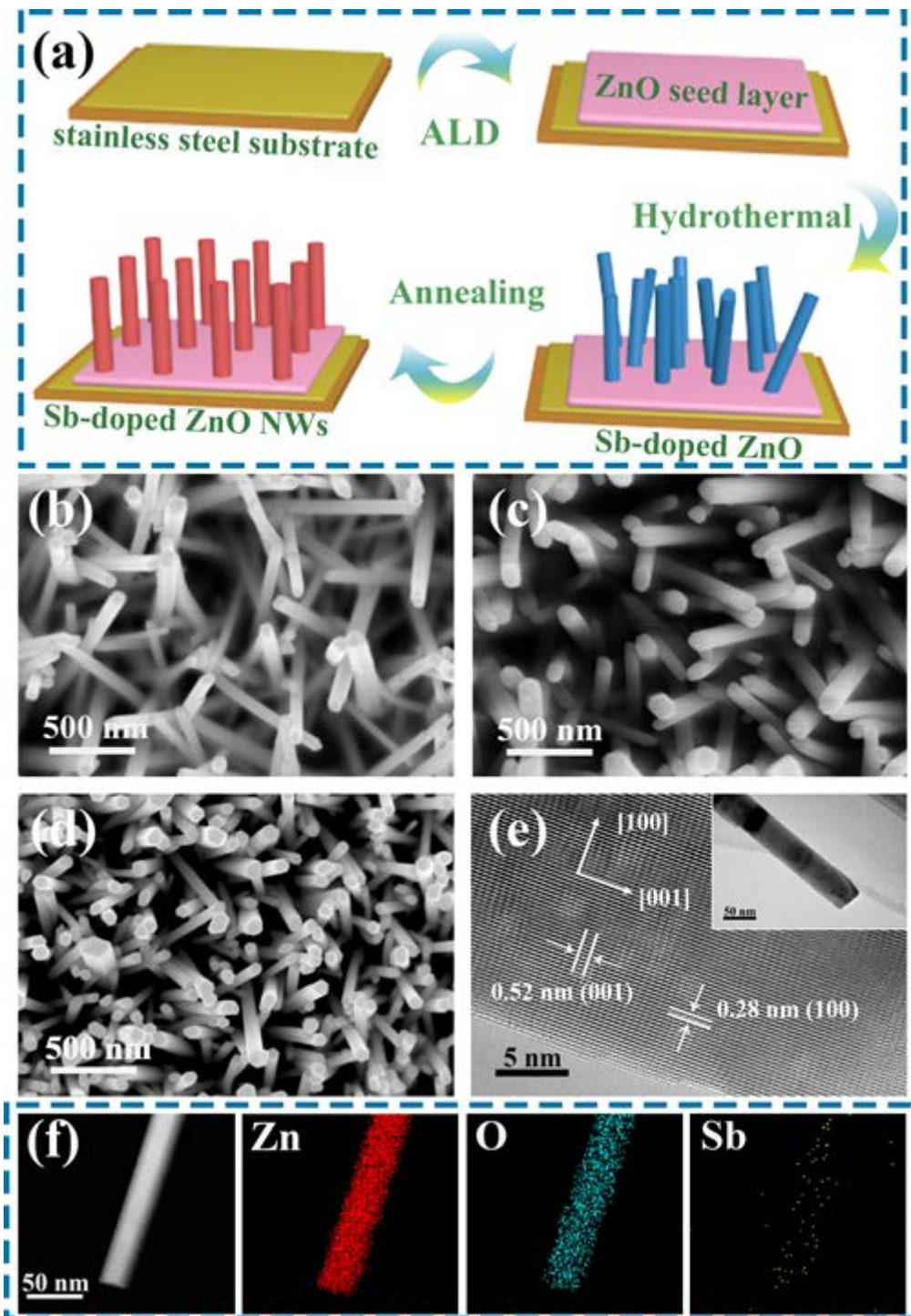
Fig. 1. (a) Schematic fabrication process of Sb-doped ZnO NWs. SEM images of (b) n-ZnO, (c) 0.2Sb/ZnO and (d) 0.2Sb/ZnO-anneal NWs samples; (e) TEM (inset) and HRTEM images of 0.2Sb/ZnO-anneal NWs samples; (f) EDS elemental mapping images recorded on the 0.2Sb/ZnO-anneal NWs samples taken by TEM.

To study the microstructure and substance components, TEM images were acquired as presented in Fig. 1e. The TEM image of the 0.2Sb/ZnO-anneal NWs

displays well-crystallized structure and clean surface in agreement with the view of SEM images. The high-resolution TEM (HRTEM) graph proves a distinct lattice spacing about 0.28 nm relevant to the (100) planes of the wurtzite ZnO in Fig. 1e. The interplanar spacing (0.52 nm) corresponds to the (001) plane in the 0.2Sb/ZnO-anneal sample [39,42]. Furthermore, the EDS mapping images (Fig. 1f) of the 0.2Sb/ZnO-anneal NWs confirm the existence of individual elements such as Zn, O and Sb, which proves the uniform Sb doping into ZnO NWs. The results indicate that highly-ordered Sb-doped ZnO NWs can be produced by the simple hydrothermal method.

The ultraviolet-visible diffuse reflectance spectra (UV-vis) of undoped and Sb-doped ZnO NWs are displayed in Fig. 2a. Compared to the undoped ZnO NWs, the absorption edge of ZnO NWs with different Sb doping concentrations shows an obvious red shift. In the corresponding Tauc plots (inset in Fig. 2a) [43], the obtained band gap value of 0.2Sb/ZnO-anneal NWs (2.99 eV) is decreased by 0.15 eV with respect to the undoped ZnO NWs (3.14 eV), which is basically owing to Sb doping . In the Sb-doped ZnO NWs sample, the new defect states may be introduced above the ZnO valence band and formed the defect band whose width is determined by the amount of Sb doping [44,45]. Electrons is photogenerated directly from the defect band to the conduction band, which might be the main reason for the reduced band gap relative to the undoped ZnO NWs.
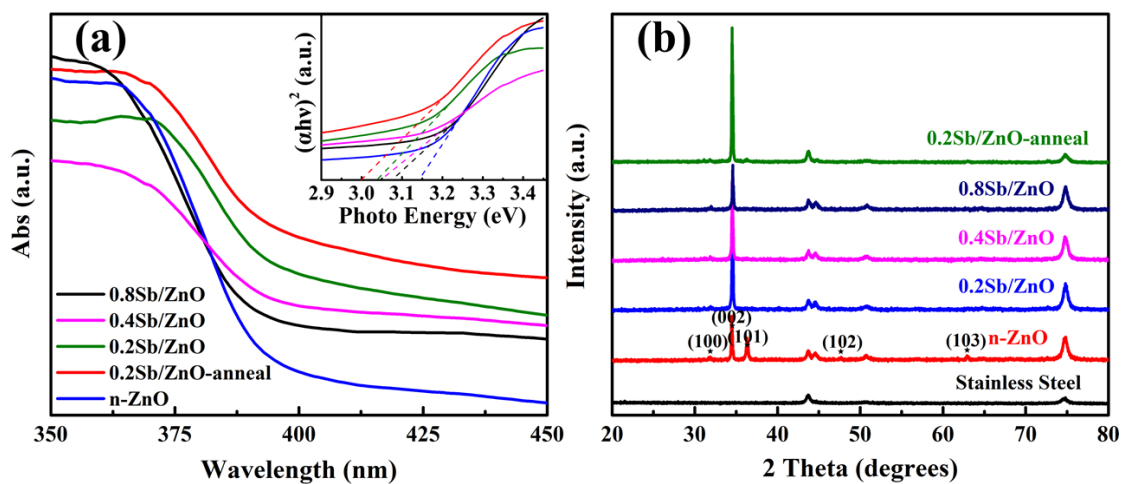

Fig. 2. (a) UV-vis absorption spectra and (b) XRD patterns of n-ZnO, 0.2Sb/ZnO, 0.4Sb/ZnO, 0.8Sb/ZnO and 0.2Sb/ZnO-anneal samples. The inset in (a) presents the corresponding plots of $(\alpha h\nu)^2$ vs. photon energy.

Fig. 2b presents the crystal structure of ZnO NWs treated under different experimental conditions. The XRD patterns confirm that all the peaks related to ZnO are indexed to the standard hexagonal phase wurtzite structure. There are no additional impurity diffraction peaks observed, which could be due to the low Sb doping content and most Sb ions occupying the positions inside the ZnO lattice. The diameter of ZnO NWs appears a significant increase after Sb doping. With Sb doping and annealing treatment, the intensities of (100) and (101) peaks of ZnO decrease, while that of (002) peak significantly enhances, corresponding to the well-defined [001] growth direction. These changes indicate that the 0.2Sb/ZnO-anneal NWs possess better crystallinity and orientation, showing a well-structured c-axis preferred orientation [46-47]. The well-orientation ZnO NWs with specific crystal faces are beneficial for achieving piezotronic effect which can effectively regulate the charge separation and transfer to improve PEC performance later. Moreover, Raman spectra are shown in Fig. S1 (Supporting Information, SI). A common Raman peak at 437 cm^{-1} is corresponding to the E_2^{high} vibrational mode which demonstrates the typical wurtzite structure for undoped ZnO and Sb-doped ZnO samples. The 333 cm^{-1} peak is related to the $E_2^{high} - E_2^{low}$. After Sb doping into ZnO NWs, a new Raman peak centered at 712 cm^{-1} can be observed in a weak intensity due to the weak local vibration mode associated with the Sb-O oscillation [21,39].

In order to analyze the chemical constitutions and oxidation states of the undoped and Sb-doped ZnO samples, XPS spectra were collected and displayed in Fig. 3(a-d). Fig. 3a exhibits the survey XPS spectrum of the 0.2Sb/ZnO-anneal sample that manifests the existence of the elements Zn, O, Sb and extraneous C. As shown in Fig. 3b, two strong peaks at 1021.4 and 1044.4 eV belong to the Zn $2p_{3/2}$ and Zn $2p_{1/2}$ states, respectively. The O 1s spectrum in Fig. 3c can be deconvoluted into two peaks at 530.3 and 531.3 eV, which may be attributed to the oxygen atoms coordinated with Zn atoms and hydroxyl oxygen on the sample surface, respectively. According to the previous report [21], the hydroxyl oxygen was a necessary source applied to the photocatalytic activity.

Furthermore, the Sb 3d states of 0.2Sb/ZnO-anneal photoelectrode could be

presented by the XPS peaks at 530.3 and 539.8 eV (inset of Fig. 3d). However, the peak located at 530.3 eV corresponding to Sb $3d_{5/2}$ states is overlapped with the O 1s peaks. It is difficult to accurately distinguish the Sb $3d_{5/2}$ peak from the O 1s region. Thus, the successfully doping of Sb elements in ZnO structure and the formation of Sb-O bond could be demonstrated by the other characteristic Sb 3d3/2 peak which is located at around 539.8 eV. The Sb $3d_{3/2}$ XPS peak can be deconvoluted into two peaks indicating that the co-existence of two Sb valence states including Sb^{3+} centered at 539.2 eV and Sb^{5+} at 539.9 eV [48]. It was reported by Limpijumnong et al. that the Sb atoms would substitute Zn sites with the introduction of two zinc vacancies (V_{Zn}) to form the shallow acceptor Sb_{Zn}-$2V_{Zn}$ complex in ZnO [49]. Based on the research, the Sb valence state might be Sb^{5+} and Sb^{3+} within the Sb_{Zn}-$2V_{Zn}$ complex leading to the 1- and 3- charge complex. Although both can account for our p-type conduction result, the strong XPS peak at 539.9 eV suggests that the main charge state of Sb dopant is Sb^{5+} in the p-type conductivity [19]. This can be further confirmed by theoretical calculation on the defect formation energy later (Table 1). The XPS results of the ZnO samples with different Sb concentrations are also presented in Fig. S2.
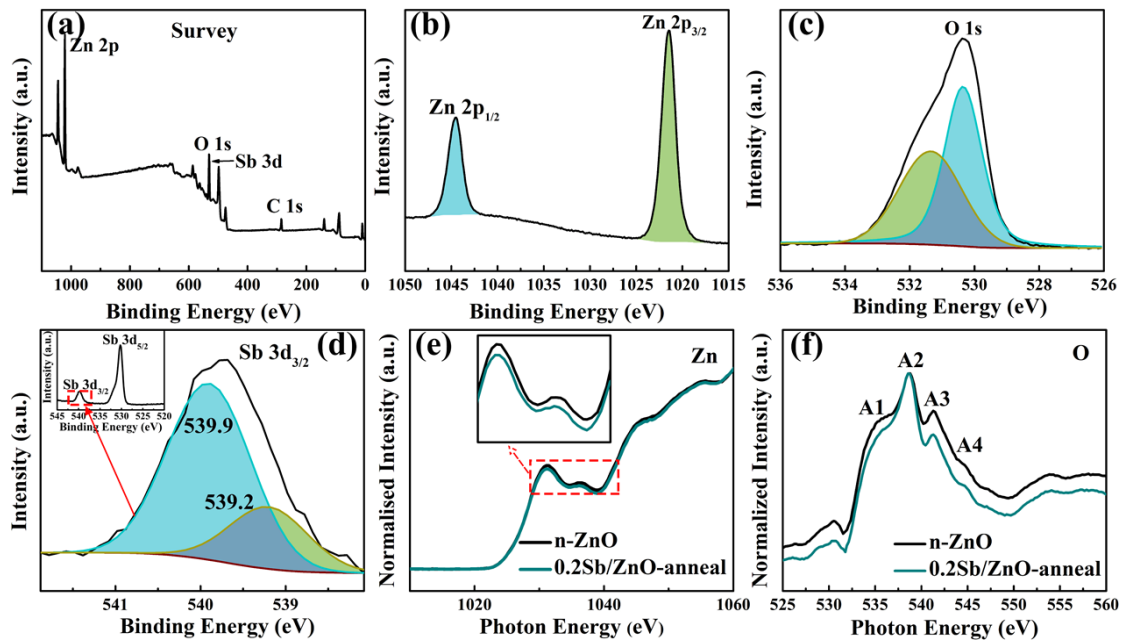

Fig. 3. XPS spectra of the 0.2Sb/ZnO-anneal sample: (a) Survey scan, (b) Zn 2p peaks, (c) O 1s peak, (d) Sb 3d peak (inset) and Sb $3d_{3/2}$ peak. (e) Zn $L_{3,2}$-edge XANES spectra of n-ZnO and 0.2Sb/ZnO-anneal sample. The inset shows the magnified view of the

XANNES. (f) O K-edge XANES spectra for n-ZnO and 0.2Sb/ZnO-anneal NWs sample.

The XANES spectra of n-ZnO and 0.2Sb/ZnO-anneal NWs at the Zn $L_{3,2}$-edge and O K-edge are presented in Figs. 3e and f, respectively. As shown in Fig. 3e, the intensity of 0.2Sb/ZnO-anneal NWs decreases in comparison to the n-ZnO NWs after the normalization. This indicates that the valence state of Zn sites has a decreasing trend after Sb doping into ZnO, and suggests the formation of the Sb_{Zn}-$2V_{Zn}$ complex [50,51], which is consistent with the XPS results. Furthermore, as shown in the O K-edge XANES spectra in Fig. 3f, the 530-539 eV energy region (labeled A1-A2) is mainly attributed to the hybridization between the O 2p electronic state and the highly dispersed Zn 3d/4s state. The weaker A1 peak in the pre-edge region of 0.2Sb/ZnO-anneal sample relative to the n-ZnO sample indicates the presence of V_{Zn} and Sb_{Zn} in the ZnO lattice [52-54]. Therefore, the XANES results further support the formation of the Sb_{Zn}-$2V_{Zn}$ complex in the Sb-doped ZnO samples.

The PL spectra are presented in Figs. 4a and S3 with the excitation wavelength at 325 nm. The peak located at 395 nm is correlated with the near band edge (NBE) emission in ZnO NWs. The PL intensity gradually decreases with the Sb doping concentration in the ZnO NWs, which suggests more efficient photogenerated electron-hole separation [55-56]. In comparison to the 0.2Sb/ZnO NWs, the PL peak of the 0.2Sb/ZnO-anneal NWs displays an obvious red shift. Such PL peak and can be carefully deconvoluted into three peaks centered at 395, 417 and 461 nm, where the 395 nm peak comes from NBE emission while the latter two peaks may be associated with the generated Sb_{Zn}-$2V_{Zn}$ complex and result from the Sb doping and thermal treatment of the ZnO NWs. Based on the report by Tian et al. [57], the complex defect state is centered at 0.16 eV above the valence band maximum (VBM) and the band gap E_g of the ZnO NWs prepared above is 3.14 eV. Thus, the result of $E_g - 0.16 = 2.98$ eV is similar to the emission energy of the PL peak at 417 nm (2.97 eV) for the 0.2Sb/ZnO-anneal sample. The result demonstrates that this emission is attributed to the energy difference from the conduction band to the complex level (as shown in Fig. 4b). Some previous reports suggested that the energy difference between the Zn_i level and the

complex level is 2.71 eV [58]. So, the peak located at 461 nm might be owing to the transition from the Zn_i level to the complex level. The intensity of the emission peak located at 417 nm is larger than the peak at 461 nm, which confirms the dominant effect of the Sb_{Zn}-$2V_{Zn}$ complex in the 0.2Sb/ZnO-anneal sample. Based on the discussion above, the formation of p-type ZnO comes from the proper Sb doping into ZnO NWs and the generation of the Sb_{Zn}-$2V_{Zn}$ complex which can compensates and overwhelms the effects of native defects such as V_O and Zn_i by annealing.
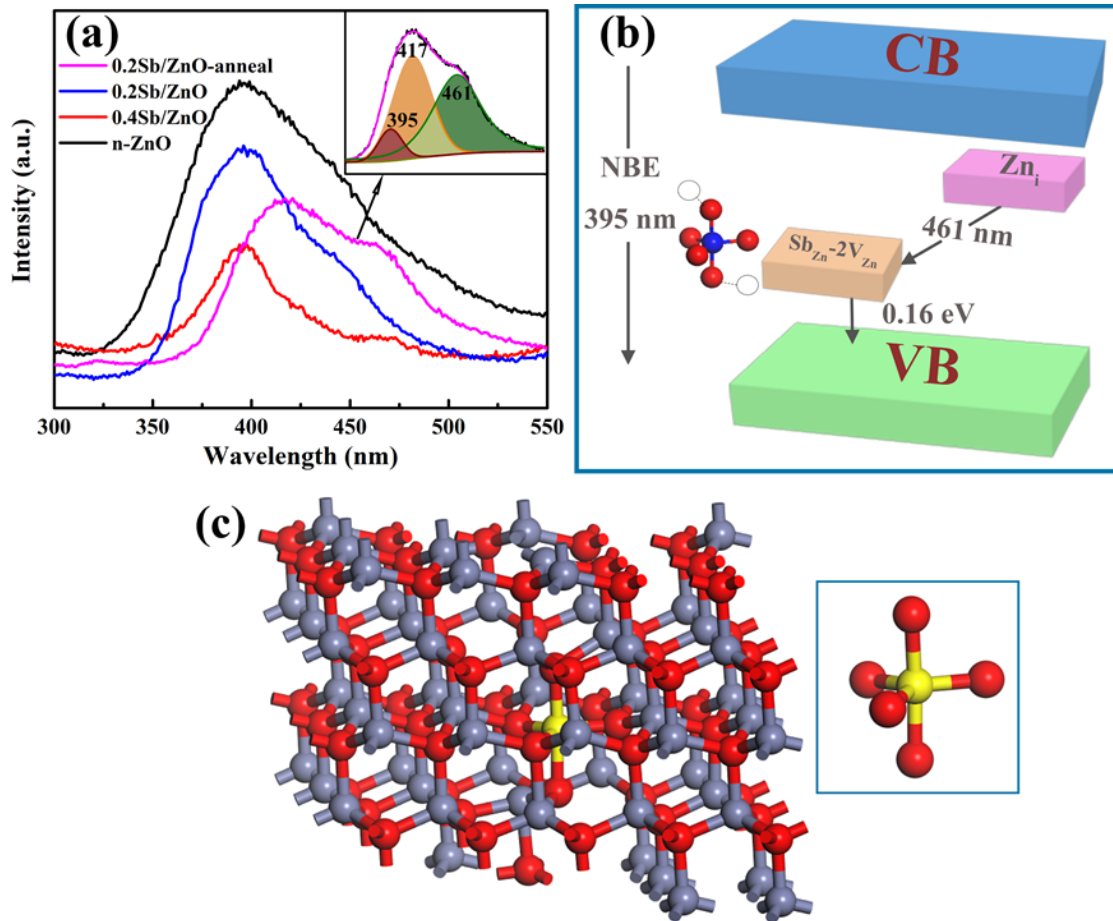

Fig. 4. (a) PL spectra of n-ZnO, 0.2Sb/ZnO, 0.4Sb/ZnO and 0.2Sb/ZnO-anneal NWs samples. Inset shows the fitted PL spectra of 0.2Sb/ZnO-anneal sample. (b) Proposed schematic of energy levels for 0.2Sb/ZnO-anneal sample. (c) Atomic structure of the Sb_{Zn}-$2V_{Zn}$ complex in ZnO structure after relaxation. The red, gray and yellow spheres are O, Zn and Sb atoms, respectively. The inset shows the fivefold structure between the Sb and O after Sb doping.

Table 1. Defect formation energies of different charged states.

Charge	q	E_{total}^d	E_{total}^p	$E_{(Zn)}$	$E_{(Sb)}$	E_F	E_f
Sb^{5+}	-1	539.582				-0.14	1.95
			-546.46	-4.175	-7.465		
Sb^{3+}	-3	539.434				-0.28	2.77

In order to further prove the formation of the Sb$_{Zn}$-2V$_{Zn}$ complex with Sb^{5+} state, we constructed a defect model (Fig. 4c) by DFT calculations using a 5 x 3 x 2 super cells and investigated the formation energies of 1- (corresponding to Sb^{5+}) and 3- (corresponding to Sb^{3+}) charged states, respectively. When Sb dopes into ZnO, the fourfold structure voluntarily changes to the fivefold structure without any energy barrier (the defect model before structural optimization is shown in Fig. S4) [49]. The defect formation energy was obtained based on the following equation [59]:

$$E_f$$
$$= E_{total}^d - E_{total}^p + 3E_{(Zn)} - E_{(Sb)}$$
$$+ qE_F \tag{1}$$

where E_{total}^d is the total energy of the supercell structure with the defects, E_{total}^p is the energy of a perfect equivalent supercell, q and E_F are the charge of the defect and their Fermi level position concerning the VBM. The defect formation energies for the 1- and 3- charged states are presented in Table 1. The formation energy for the 1- charged Sb$_{Zn}$-2V$_{Zn}$ complex is 1.95 eV, which is relatively low with respect to the 3- charge complex (2.77 eV). This confirms the preferential formation of the Sb$_{Zn}$-2V$_{Zn}$ complex with Sb^{5+} state and is in good agreement with the XPS result in Fig. 3d. Furthermore, the total and partial density of states (DOS) of the 1- and 3- charged Sb$_{Zn}$-2V$_{Zn}$ complex are shown in Fig. S5. The overlap between the Sb 5p and Zn 3d orbits is relatively intense in the 1- charge complex, indicating the enhancement of the orbit hybridization. This is mainly due to the large positive charge of the Sb$_{Zn}$ state in the 1- charge complex, which can strengthen the attraction between the V$_{Zn}$ and Sb$_{Zn}$ states. The V$_{Zn}$ in the complex introduces the acceptor levels, and strong hybridization between the Sb 5p and Zn 3d orbits could reduce the influence of the repulsive potential among the acceptors, which is beneficial to the conductivity improvement of Sb-doped

p-type ZnO NWs [60].

Whether the Sb-doped ZnO NWs are p-type conductivity can be determined by Mott-Schottky plots as exhibited in Fig. 5. For the undoped ZnO NWs, the slope of the Mott-Schottky plot exhibits an obviously positive slope (inset in Fig. 5a) that shows the typical characteristic of n-type conductivity. However, the negative slopes of ZnO NWs with different Sb doping concentrations are observed in Figs. 5(a-b), indicating the successful preparation of p-type ZnO NWs photoelectrodes [56]. The free carrier density (N_D) of the photoelectrodes can be calculated by the following equation [61]:

$$N_D = \frac{2}{e \varepsilon_0 \ \varepsilon_r} \left(\frac{dE}{d\left(\frac{1}{C^2}\right)} \right) \tag{2}$$

where e is the charge on the electron (1.6×10^{-19} C), ε_0 is the permittivity of free space (8.86×10^{-12} F/m), and ε_r is the relative permittivity of ZnO (8.5). N_D values of the n-ZnO, 0.2Sb/ZnO, 0.4Sb/ZnO, 0.8Sb/ZnO and 0.2Sb/ZnO-anneal photoelectrodes were calculated to be 6.88×10^{15}, 5.95×10^{16}, 4.88×10^{16}, 2.94×10^{16} and 9.37×10^{16} cm^{-3}, respectively. Therefore, Sb doping and thermal treatment can lead to an increase of carrier density in the 0.2Sb/ZnO-anneal photoelectrode which may account for enhanced PEC performance [62].
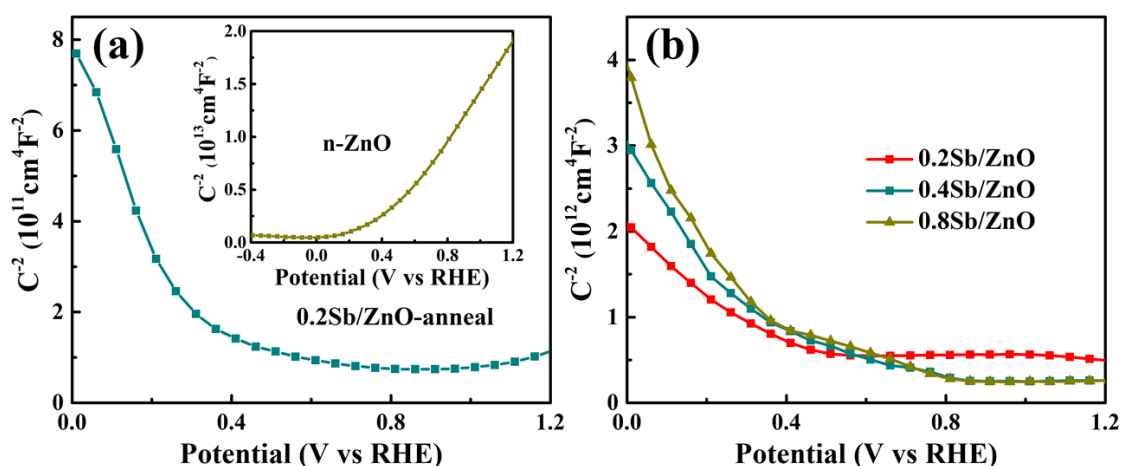

Fig. 5. Mott-Schottky plots of (a) 0.2Sb/ZnO-anneal sample, n-ZnO sample (inset), (b) 0.2Sb/ZnO, 0.4Sb/ZnO and 0.8Sb/ZnO samples measured at 1 kHz in dark.

Fig. 6 presents the PEC properties of the ZnO NWs samples. The linear sweep voltammetry (LSV) curves were tested under illumination condition and in dark, as

shown in Fig. 6a. The cathodic photocurrent density is relatively low for n-ZnO NWs. The photocurrent density of the Sb-doped ZnO photoelectrodes increases as the Sb doping concentration rises to 0.2 mol%. After that, the photocurrent density decreases with the increasing Sb doping concentration (Fig. S6). The 0.2Sb/ZnO NWs exhibits a better photocurrent density that reaches -0.25 mA/cm^2 at 0 V$_{RHE}$, which is 5 times higher than the undoped ZnO NWs (0.05 mA/cm^2 at 0 V$_{RHE}$). After the annealing process, the 0.2Sb/ZnO-anneal photoelectrode demonstrates the maximal PEC behavior and the photocurrent density can reach -0.85 mA/cm^2 at 0 V$_{RHE}$, which is 3.3 times higher than that of the 0.2Sb/ZnO sample. The LSV curves of ZnO with different Sb doping concentration and n-ZnO samples under annealing treatment are displayed in Fig. S7. The significant PEC enhancement can be attributed to the high carrier density and effective electron/hole separation and transfer that come from the improvement of the crystal quality, decrease of native donor defects and formation of the Sb$_{Zn}$-2V$_{Zn}$ complex after Sb doping and thermal treatment [21,63].
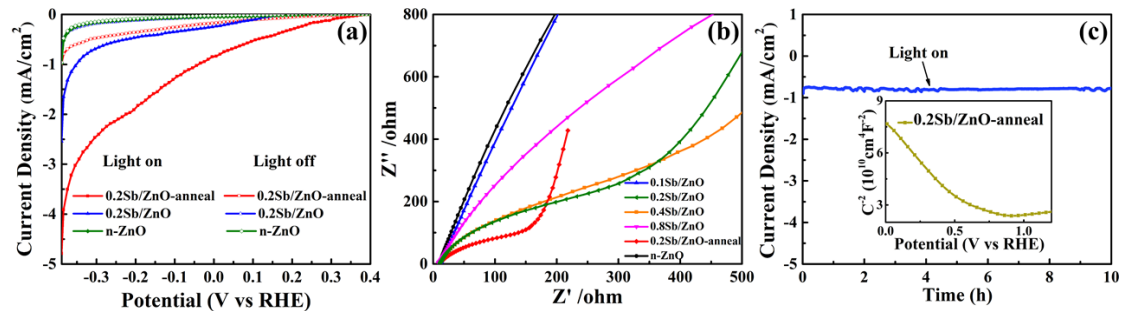

Fig. 6. (a) LSV curves of n-ZnO, 0.2Sb/ZnO and 0.2Sb/ZnO-anneal photoelectrodes under simulated sunlight illumination and in dark. (b) EIS Nyquist plots using 10 mV vibration potential amplitude under light irradiation. (c) The photocurrent density versus time of 0.2Sb/ZnO-anneal photoelectrode at 0 V$_{RHE}$. The inset shows the Mott-Schottky plots of 0.2Sb/ZnO-anneal photoelectrode after 10 h continuous working.

EIS Nyquist plots were also implemented to investigate the interfacial charge transfer performance of the photoelectrodes at different preparation conditions as presented in Fig. 6b. The measurement was conducted with 10 mV amplitude perturbation in 0.2 M Na$_2$SO$_4$ solution under simulated sunlight irradiation. The charge transfer resistance across the interface (R_{ct}) can be expressed by the semicircle diameter

of the arc in Nyquist plots using the Randles-Ershler model. The arc for the 0.2Sb/ZnO-anneal photoelectrode is smallest in the undoped and Sb-doped ZnO photoelectrodes, illustrating the most efficient charge transfer across the interface to the electrolyte and suppression of charge recombination [64,65]. Previous work reported that the as-prepared p-type ZnO photoelectrode was unstable and easy to convert to n-type conductivity under ordinary conditions [7]. However, the stability of the p-type Sb-doped ZnO NWs is excellent in our work. Fig. 6c shows the photocurrent density response of 0.2Sb/ZnO-anneal sample within continuous illumination of 100 mW/cm^2 for 10 h at 0 V$_{RHE}$. The photoelectrode shows a steady average photocurrent density of -0.82 mA/cm^2 without degradation under constant irradiation for over 10 h at 0 V$_{RHE}$. The Mott-Schottky plot in the inset of Fig. 6c indicates that the p-type conductivity remains unchanged after 10 h constant illumination. Wang et al. reported that the p-type conductivity could keep only 2 months in the as-prepared p-type ZnO NWs [66]. Fig. S8 displays the comparison of PEC performance of the 0.2Sb/ZnO-anneal sample before and after 6-month storage. The photocurrent density is only slightly reduced after 6 months, and the sample remains p-type behavior.
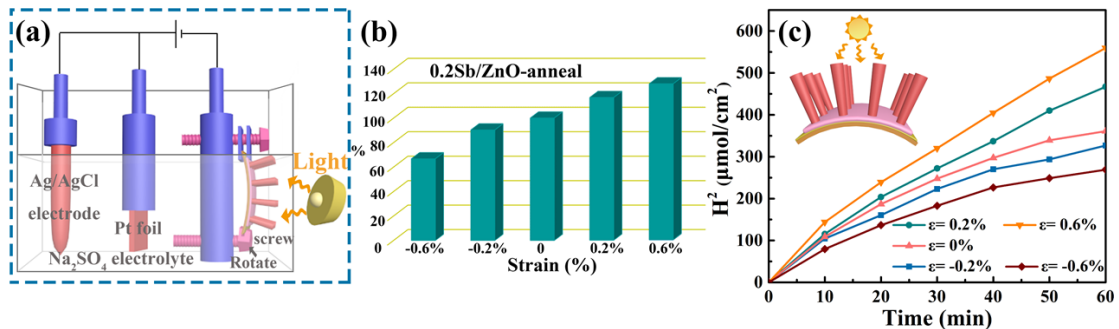
3.2 Piezotronic Effect in p-type ZnO NWs

Fig. 7. (a) Schematic setup of the PEC system for characterizing the piezotronic effect acting on water splitting reactions. (b) Photocurrent density change rate for 0.2Sb/ZnO-anneal sample by applying different strains under a bias of 0 V$_{RHE}$. (c) Time course of H$_2$ evolution at -0.2 V$_{RHE}$ by 0.2Sb/ZnO-anneal photoelectrode under different strains.

To further emphasize the regulation of PEC performance using the piezotronic effect in p-type ZnO NWs, a specially designed electrode holder was used in a three-electrode PEC system to adjust the strain in ZnO NWs during the measurements as

shown in Fig. 7a. The exposed area on ZnO NWs surface was a 0.5×0.5 cm^2 working area for the water reduction reaction. The upper part of the working electrode was clamped by two gaskets and fixed on the electrode holder by a screw. The bottom part was connected to the electrode holder by a special screw that could achieve different strains by rotating the two screws. The magnitude of the strain can be calculated by the vertical variable of the bottom screw. The piezoelectric coefficients (e_{33}) for the undoped and Sb-doped ZnO samples were obtained by DFT calculations and presented in Table 2. The Sb-doped ZnO NWs sample with Sb^{5+} charge states in the Sb$_{Zn}$-2V$_{Zn}$ complex has the highest piezoelectric constant in comparison to the undoped and Sb-doped ZnO NWs with Sb^{3+} charge state. This thus can be expected to significantly improve PEC performance by doping Sb into ZnO NWs. Hence, we choose the 0.2Sb/ZnO-anneal sample for piezotronic effect measurements.

Table 2 Piezoelectric Constants of undoped and Sb-doped ZnO samples.

	Undoped ZnO		Sb-doped ZnO	
	Our work	References	Sb^{5+}	Sb^{3+}
e_{33}		0.96 [67]		
	1.14	1.01 [68]	3.73	2.08
		1.34 [69]		

The LSV curves of the 0.2Sb/ZnO-anneal sample are presented in Fig. S9 under different strains. According to the previous report [37], the tensile strain values were defined as positive and compressive strain values were defined as negative. With the variation of strain, the photocurrent density correspondingly increased or decreased. Fig. 7b shows the change rate of photocurrent density in the 0.2Sb/ZnO-anneal sample under a bias of 0 V$_{RHE}$. When a 0.6% tensile strain was applied, the photocurrent density of the 0.2Sb/ZnO-anneal sample reaches -1.08 mA/cm^2, which is 27.4% enhancement in comparison to the sample without strain. The 0.2Sb/ZnO-anneal sample under a 0.6% tensile strain can reach the maximum STH efficiency ($\eta = 0.1\%$) at 0.2 V$_{RHE}$, which is 66.7% higher than the photoelectrode without applying any strain [70]. Future work can be carried out to further improve the STH efficiency, such as through introducing

co-catalysts, etc. The opposite result was observed by applying 0.6% compressive strain, and the photocurrent density is reduced by 33.3%. These changes indicate that the piezotronic effect can effectively regulate the PEC performance on p-type ZnO NWs [26]. The photocatalytic performance was also measured by evaluating the hydrogen evolution property as shown in Fig. 7c. Compared with the 0.2Sb/ZnO-anneal photoelectrode without strain, the photoelectrode demonstrates apparently different photoactivity under different strains. The ZnO NWs under 0.6% tensile strain exhibit the superior H_2 generation rate of 559.5 μmol/cm^2 after 1 hour with the Faradaic efficiency (FE) of 86.3% [71]. However, the photocatalytic performance of the p-type ZnO NWs under compressive strains shows a 25.4% decrease of hydrogen production with respect to the ZnO NWs without strain. Thus, PEC H_2 generation activity of the p-ZnO NWs can be controlled by applying different strains, which demonstrates the effective modulation of PEC behavior by the piezotronic effect through controlling the separation and transfer of charge carriers in p-type ZnO NWs.
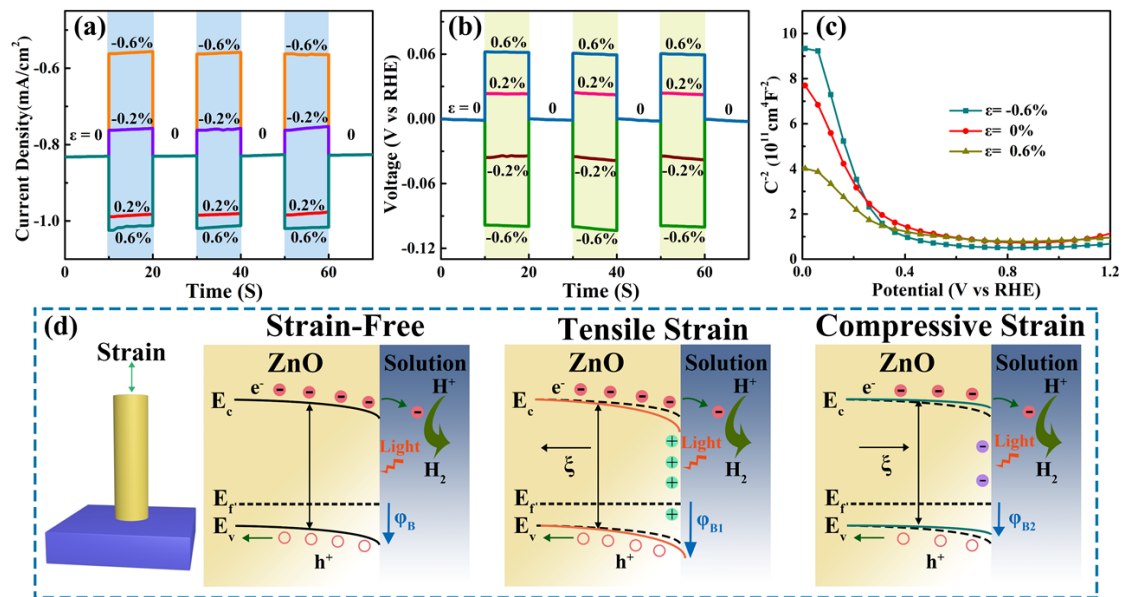

Fig. 8. (a) Photocurrent density of 0.2Sb/ZnO-anneal sample at 0 V_{RHE} by applying periodical strains under illumination of 100 mW/cm^2. (b) Applied bias (V) under periodical strains with 100 mW/cm^2 light irradiation. The photocurrent density was kept at -0.85 mA/cm^2. (c) Mott-Schottky plots of 0.2Sb/ZnO-anneal sample with or without strains. (d) Schematic band diagrams of 0.2Sb/ZnO-anneal sample without strain, with tensile strain and compressive strain. The dash lines showing the band bending displays

the reference energy band without stain.

We further examine the reproducibility of piezotronic effect on the 0.2Sb/ZnO-anneal sample. Fig. 8a shows the photocurrent density of the 0.2Sb/ZnO-anneal sample at 0 V_{RHE} by applying periodical strains. Photocurrent response to strains is rapid and reproducible. The transient photocurrent curves at a bias of 0 V_{RHE} was observed that demonstrates the strain-induced changes are constant (Fig. S10). Fig. 8b displays the galvanostatic test on the 0.2Sb/ZnO-anneal sample, which can show the piezotronics effect alters the applied bias in order to accomplish the same photocurrent density. The applied bias rises from 0 V_{RHE} to -0.098 V_{RHE} when subjected to compressive strain (-0.6%) indicating that a higher bias is required to maintain the photocurrent constant by applying compressive strain. From Fig. 8c, the slopes of Mott-Schottky plots are still negative with or without strain applied to the ZnO NWs, suggesting the piezotronic effect will not change the p-type conductivity of ZnO NWs. The N_D values of the 0.2Sb/ZnO-anneal photoelectrode under 0.6% tensile strain is 1.69×10^{17} cm^{-3} that shows more carriers can be produced to improve PEC performance under tensile strain.

To fully understand the influence of the piezotronic effect on the charge separation and transfer in the ZnO photoelectrode, the band structure diagrams are presented in Fig. 8d to clarify the underlying mechanism. Fig 8d shows the band diagram of 0.2Sb/ZnO-anneal photoelectrode without strain. A Schottky barrier is formed at the interface between the p-ZnO and electrolyte. Under light illumination, photogenerated electron-hole pairs separate in the ZnO NWs due to the inclined band. When tensile strain is applied on the ZnO NWs along the c-axis, the positive piezo-electric polarization charges are generated at the ZnO-electrolyte interface owing to the piezotronic effect. The polarization-induced positive piezoelectric potential strengthens the valence band and conduction band energy downward bending at the ZnO-electrolyte interface. Therefore, a strong local electric field is introduced by the tensile strain on the interface, which can effectively separate the electron-hole pairs to decrease the recombination rate and further enhance the PEC performance [26,72,73]. On the other hand, when the compressive strain is applied to the ZnO NWs, the induced negative piezoelectric potential at the interface results in upward band bending, which

corresponds to a reduced PEC performance.

4. Conclusions

In summary, we have demonstrated a novel way to achieve stable p-type ZnO NWs and improve the PEC performance by piezotronic effect. The p-type Sb-doped ZnO NWs with high crystallinity were prepared by a low-temperature method including ALD, hydrothermal method and thermal treatment. Systematic characterizations and theoretical calculation confirm Sb ions occupying Zn sites and forming the Sb_{Zn}-$2V_{Zn}$ complex. The p-type behavior is affirmed by the Mott-Schottky plots. The p-type ZnO NWs exhibit more efficient photogenerated electrons-holes separation and transfer compared with the undoped ZnO sample. The photocurrent density can reach -0.85 mA/cm^2 (0 V_{RHE}) that is 17.2 times larger than the n-ZnO NWs under simulated sunlight illumination. The piezotronic effect can be introduced and tuned by applying different strains on the p-type ZnO NWs through a self-designed device in the PEC measurements, where the photocurrent density can be further improved up to 27.4% under a 0.6% tensile strain without changing the conductivity characteristics. The piezotronic effect can continuously improve PEC performance by significantly accelerating charge separation and transfer through modulating the band structure near the interface. This work puts forward an efficient way to design and develop high-performance photoelectrode toward PEC hydrogen evolution. Besides, it extends the applications of piezotronic effect for enhancing the efficiency of optoelectronics and piezotronics.

Zheng from the National Synchrotron Radiation Laboratory for their help in XPS and XANES characterizations, respectively.

References

[1]   A. Fujishima, K. Honda, Nature 238 (1972) 37–38.

[2]   H. Ma, W. Ma, J.F. Chen, X.Y. Liu, Y.Y. Peng, Z.Y. Yang, H. Tian, Y.T. Long, J. Am. Chem. Soc. 140 (2018) 5272-5279.

[3]   Z.M. Bai, X.Q. Yan, Y. Li, Z. Kang, S.Y. Cao, Y. Zhang, Adv. Energy Mater. 6 (2016) 1501459.

[4]   S.Y. Cao, X.Q. Yan, Z. Kang, Q.J. Liang, X.Q. Liao, Y. Zhang, Nano Energy 24 (2016) 25-31.

[5]   J.B. Cui, L.Q. Shi, T.F. Xie, D.J. Wang, Y.H. Lin, Sens. Actuators B: Chem. 227 (2016) 220-226.

[6]   K.K. Liu, X.M. Li, S.B. Cheng, R. Zhou, Y.C. Liang, L. Dong, C.X. Shan, H.B. Zeng, D.Z. Shen, Nanoscale 10 (2018) 7155-7162.

[7]   S.D. Baek, P. Biswas, J.W. Kim, Y.C. Kim, T.I. Lee, J.M. Myoung, ACS Appl. Mater. Interfaces 8 (2016) 13018-13026.

[8]   U. Ozgur, Y.I. Alivoy, C. Liu, A. Teke, M.A. Reshchikov, S. Dogan, V. Avrutin, S.J. Cho, H. Morkoc. J. Appl. Phys. 98 (2005) 041301.

[9]   A. Janotti, C.G.V.d. Walle, Rep. Prog. Phys. 72 (2009) 126501

[10] J. Qu, Y.R. Ge, B.Y. Zu, Y.X. Li, X.C. Dou, Small 12 (2016) 1369-1377.

[11] P. Sharma, R. Bhardwaj, R. Singh, S. Kumar, S. Mukherjee, Appl. Phys. Lett. 111 (2017) 091604.

[12] Z.Z. Ye, H.P. He, L. Jiang, Nano Energy 52 (2018) 527-540,

[13] J.C. Fan, K.M. Sreekanth, Z. Xie, S.L. Chang, K.V. Rao, Prog. Mater Sci. 58 (2013) 874-985.

[14] R. Mannam, S.K. Eswaran, N. Dasgupta, M.S.R. Rao, Appl. Surf. Sci. 347 (2015) 96-100.

[15] C.L. Hsu, K.C. Chen, T.Y. Tsai, T.J. Hsueh, Sensor. Actuat. B-Chem. 182 (2013) 190-196.

[16] Z.F. Shi, Y.T. Zhang, B. Wu, X.P. Cai, J.X. Zhang, X.C. Xia, H. Wang, X. Dong, H.W. Liang, B.L. Zhang, G.T. Du, Appl. Phys. Lett. 102 (2013) 161101.

[17] A.P. Bhirud, S.D. Sathaye, R.P. Waichal, L.K. Nikam, B.B. Kale, Green Chem. 14 (2012) 2790-2798.

[18] W.J. Chen, J.K. Wu, J.C. Lin, S.T. Lo, H.D. Lin, D.R. Hang, M.F. Shih, C.T. Liang, Y.H. Chang, Nanoscale Res. Lett. 1 (2013) 313.

[19] T. Yang, B. Yao, T.T. Zhao, G.Z.Xing, H. Wang, H.L.Pan, R. Deng, Y.R. Sui, L.L. Gao, H.Z.Wang, T. Wu, D.Z. Shen, J. Alloys Compd. 509 (2011) 5426-5430.

[20] X.L. Ren, X.H. Zhang, N.S. Liu, L. Wen, L.W. Ding, Z.W. Ma, J. Su, L.Y. Li, J.B. Han, Y.H. Gao, Adv. Funt. Mater. 14 (2015) 2182-2188.

[21] R. Nasser, W.B.H. Othmen, H. Elhouichet, M. Ferid, Appl. Surf. Sci. 393 (2017) 486-495.

[22] X.B. Chen, S.H. Shen, L.J. Guo, S.S. Mao, Chem. Rev. 110 (2010) 6503-6570.

[23] R. Shi, Y.H Cao, Y.J Bao, Y.F. Zhao, G.I.N. Waterhouse, Z.Y. Fang, L.Z. Wu, C.H. Tung, Y.D. Yin, T.R. Zhang, Adv. Mater. 29 (2017) 1700803.

[24] X.Q. Fang, J.X. Liu, V. Gupta, Nanoscale 5 (2013) 1716-1726.

[25] J. Shi, M.B. Starr, X.D. Wang, Adv. Mater. 24 (2012) 4683-4691.

[26] J. Shi, M.B. Starr, H. Xiang, Y. Hara, M.A. Anderson, J.H. Seo, Z.Q. Ma, X.D. Wang, Nano Lett. 11 (2011) 5587-5593.

[27] M.B. Starr, X.D. Wang, Nano Energy 14 (2015) 296-311.

[28] J. Zhang, C.Y. Wang, C. Bowen, Nanoscale 6 (2014) 13314-13327.

[29] K. Zhang, M.Z. Peng, W. Wu, J.M. Guo, G.Y. Gao, Y.D. Liu, J.Z. Kou, R.M. Wen, Y. Lei, A. Yu, Y. Zhang, J.Y. Zhai, Z.L. Wang, Mater. Horiz. 4 (2017) 274-280.

[30] F. Xie, L.B. Chen, J. Chen, J.B. Liu, L.F. Wang, M.X. Chen, Y.K. Pang, X.N. Yang, G.Y. Gao, J.Y. Zhai, Z.L. Wang, Adv. Mater. 28 (2016) 3391-3398.

[31]   M.X. Chen, B. Zhao, G.F. Hu, X.S. Fang, H. Wang, L. Wang, J. Luo, X. Han, X.D. Wang, C.F. Pan, Z.L. Wang, Adv. Funct. Mater. 28 (2018) 1706379.

[32] X.D. Wang, J.H. Song, J. Liu, Z. L. Wang, Science 316 (2007) 102-105.

[33] W.Z. Wu, Y.G. Wei, Z.L. Wang, Adv. Mater. 22 (2010) 4711-4715.

[34] R.M. Yu, W.Z. Wu, Y. Ding, Z.L. Wang, ACS Nano 7 (2013) 6403-6409.

[35] K. Gupta, S. Brahma, J. Dutta, B. Rao, C.P. Liu, Nano Energy 55 (2019) 1-21.

[36] Y.R. Wang, D.Q. Zheng, L.J. Li, Y. Zhang, ACS Appl. Energy Mater. 1 (2018) 3063-3069.

[37] K.C. Pradel, W.Z. Wu, Y.S. Zhou, X.N. Wen, Y. Ding, Z.L. Wang, Nano Lett. 13 (2013) 2647-2653.

[38] F. Wang, J.H. Seo, D. Bayerl, J. Shi, H.Y. Mi, Z.Q. Ma, D.Y. Zhao, Y.C. Shuai, W.D. Zhou, X.D. Wang, Nanotechnology 22 (2011) 225602.

[39] Q. Nie, L. Yang, C. Cao, Y.M. Zeng, G.Z. Wang, C.Z. Wang, S.W. Lin, Chem. Eng. J. 325 (2017) 151-159.

[40] M. Zeng, X.E. Peng, J.J. Liao, G.Z. Wang, Y.F. Li, J.B. Li, Y. Qin, J. Wilson, A.M. Song, S.W. Lin, Phys. Chem. Chem. Phys. 18 (2016) 17404-17413.

[41] J.S. Luo, L. Steier, M.K Son, M. Schreier, M.T. Mayer, M. Gratzel, Nano Lett. 16 (2016) 1848-1857.

[42] S. Liu, Q.L. Liao, Z. Zhang, X.K. Zhang, S.N. Lu, L.X. Zhou, M.Y. Hong, Z. Kang, Y. Zhang, Nano Res. 10 (2017) 3476-3485.

[43] Y. Gao, J.L. Wang, S.Y. Mo, F.W. Wang, F. Long, Z.G. Zou, Sol. RRL 2 (2018) 1800015.

[44] P. Nakarungsee, G.S. Chen, T.S. Herng, J. Ding, I.M. Tang, S. Talabthong, J. Magn. Magn. Mater. 397 (2016) 79-85.

[45] S. Dhara, P.K. Giri, Thin Solid Films 520 (2012) 5000-5006.

[46] Y.H Han, L. Zhang, Y.F. Wang, H.M. Zhang, S.Q. Zhang, Sci. Bull. 62 (2017) 619-625.

[47] D.K. Kwon, Y. Porte, J.M. Myoung, J. Phys. Chem. C 122 (2018) 11993-12001.

[48] S.K. Pandey, S.K. Pandey, V. Awasthi, M. Gupta, U.P. Deshpande, S. Mukherijee, Appl. Phys. Lett. 103 (2013) 072109.

[49] S. Limpijumnong, S.B. Zhang, S.H. Wei, C.H. Park, Phys. Rev. Lett. 92 (2004) 155504.

[50] O.M. Ozkendir, S. Yildirimcan, A. Yuzer, K. Ocakoglu, Prog. Nat. Sci-Mater. 26 (2016) 347-353.

[51] A. Sharma, M. Varshney, H.J. Shin, B.H. Lee, K.H. Chae, S.O. Won, Mater. Chem.

Phys. 191 (2017) 129-144.

[52] Y.M. Hu, S.S. Li, C.H. Chia, Appl. Phys. Lett. 98 (2011) 052503.

[53] Y.S. Wu, X.J. Liu, D.D. Han, X.Y. Song, L. Shi, Y. Song, S.W. Niu, Y.F. Xie, J.Y. Cai, S.Y. Wu, J. Kang, J.B. Zhou, Z.Y. Chen, X.S, Zheng, X.H. Xiao, G.M. Wang, Nat. Commun. 9 (2018) 1425.

[54] Z.Y. Chen, Y. Song, J.Y. Cai, X.S. Zheng, D.D. Han, Y.S. Wu, Y.P. Zang, S.W. Niu, Y. Liu, J.F. Zhu, X.J. Liu, G.M. Wang, Angw. Chem. Int. Ed. 57 (2018) 5076-5080.

[55] R. Shi, Z. Li, H.J. Yu, L. Shang, C. Zhou, G.I.N. Waterhouse, L.Z. Wu, T.R. Zhang, ChemSusChem 10 (2017) 4650-4656.

[56] L. Pan, S.B. Wang, J.W. Xie, L. Wang, X.W. Zhang, J.J. Zou, Nano Energy 28 (2016) 296-303.

[57] S. Tian, D. Zeng, C. Xie c, X. Zhao, Mat. Letters 116 (2014) 363–366.

[58] A. Janotti, C.G. Van de Walle, Phys. Rev. B 76 (2007) 165202.

[59] R.S. Ortiz, J.K. Jha, W. Sun, G. Nyandoto, J.C. Du, N.D. Shepherd, Semicond. Sci. Technol. 29 (2014) 115019.

[60] Y.L. Li, X. Zhao, W.L. Fan, J. Phys. Chem. C 115 (2011) 3552–3557.

[61] R. O'Hayre, M. Nanu, J. Schoonman, A. Goossens, J. Phys. Chem. C 111 (2007) 4809–4814.

[62] Z.H. Zhang, Y.J. Yu, P. Wang, ACS Appl. Mater. Interfaces 4 (2012) 990–996.

[63] J.Y. Cao, T. Kako, P. Li, S.X. Ouyang, J.H. Ye, Electrochem. Commun. 13 (2011) 275-278.

[64] M. Seol, J.W. Jang, S. Cho, J.S. Lee, K. Yong, Chem. Mater. 25 (2013) 184–189.

[65] S.J. Hong, S. Lee, J.S. Jang, J.S. Lee, Energy Environ. Sci. 4 (2011) 1781.

[66] B. Xiang, P.W. Wang, X.Z. Zhang, S.A. Dayeh, D.P.R. Aplin, C. Soci, D.P. Yu, D. Wang, Nano Lett. 7 (2007) 323-328.

[67] H.Y.S. Al-Zahrani, J. Pal, M.A. Migliorato, Nano Energy 2 (2013) 1214-1217.

[68] J.H. Lee, W.J. Lee, S.H. Lee, S.M. Kim, S.J. Kim, H.M. Jang, Phys. Chem. Chem. Phys. 17 (2015) 7857-7863.

[69] P. Gopal, N.A. Spaldin, J. Electron. Mater. 35 (2006) 539-542.

[70] S.Y. Cao, X.Q. Yan, Z. Kang, Q.J. Liang, X.Q. Liao, Y. Zhang, Nano Energy 24 (2016) 25-31.

[71] C. Liu, J.Y. Tang, H.M. Chen, B. Liu, P.D. Yang, Nano Lett. 13 (2013) 2989-2992.

[72] L.F. Wang, S.H. Liu, X.L. Feng. Q. Xu, S. Bai, L.P. Zhu, L.B. Chen, Y. Qin, Z.L. Wang, ACS Nano 11 (2017) 4859-4865.

[73] L.F. Wang, S.H. Liu, Z. Wang, Y.L. Zhou, Y. Qin, Z.L. Wang, ACS Nano 10 (2016) 2636-2643.